Implicit Large Eddy Simulations of Turbulent Flow around a Square Cylinder at Re = 22,000

Kai Zeng , Zhuoneng Li, Zeeshan A. Rana, Karl W. Jenkins

PII: S0045-7930(21)00166-3
DOI: https://doi.org/10.1016/j.compfluid.2021.105000
Reference: CAF 105000

To appear in: *Computers and Fluids*

Received date: 23 November 2020
Revised date: 30 April 2021
Accepted date: 5 May 2021

Please cite this article as: Kai Zeng , Zhuoneng Li, Zeeshan A. Rana, Karl W. Jenkins , Implicit Large Eddy Simulations of Turbulent Flow around a Square Cylinder at Re = 22,000, *Computers and Fluids* (2021), doi: https://doi.org/10.1016/j.compfluid.2021.105000

Highlights

- The Implicit LES approach with 2^{nd} and 3^{nd} order WENO scheme is applied to square cylinder flow at Re=22000
- The near wall performance of 3rd order WENO ILES is comparable to conventional LES with WALE model and out-performs LES with dynamic Smagorinsky model
- Both LES and ILES face challenge in terms of small quantities such as shear wall stress
- The 2nd-order WENO scheme can also give a fair prediction over the averaged statistics such as drag coefficient, Strouhal number, recirculation length and stream-wise velocity profile with less computational time than a 3rd-order WENO scheme.

Computers & Fluids, Volume 226, August 2021, Article number 105000
DOI:10.1016/j.compfluid.2021.105000

Implicit Large Eddy Simulations of Turbulent Flow around a Square Cylinder at Re=22,000

Kai Zeng, Zhuoneng Li, Zeeshan A. Rana, Karl W. Jenkins

Centre for Computational Engineering Sciences, Cranfield University, Cranfield, Bedfordshire MK43 0AL, United Kingdom

Abstract

In this paper, the Implicit Large-Eddy Simulation (ILES) is investigated on the flow around a square cylinder incorporating an unstructured Weighted Essential Non-Oscillatory (WENO) reconstruction method for a Reynolds number of 22,000. Simulations are undertaken in the framework of open-source package OpenFOAM and additional implicit 2nd/3rd-order WENO scheme on the convective term of the viscous incompressible Navier-Stokes Equations. A 2nd-order Euler implicit time integration and Pressure-Implicit Splitting-Operator (PISO) algorithm is used to for the pressure-velocity coupling. Conventional LES with Wall Adapting Local Eddy Viscosity (WALE) model is also carried out as a baseline. The results are compared to high fidelity experiment, DNS data and conventional LES with dynamic Smagorinsky model from previous work. Results show favorable performance for ILES with 3rd-order WENO scheme compared with the conventional LES with dynamic Smagorinsky model and similar performance against LES with WALE model. Results also show acceptable predictions over time-averaged statistics with less computational effort for the ILES of 2nd-order WENO scheme. Shear layer flow analysis suggests that both ILES and LES face similar challenges with small quantities, such as shear stress. Finally, simulations are capturing Von Kármán vortex, Kelvin-Helmholtz instability and induced frequency changes.

Keywords: Implicit LES, WENO, Turbulent Flow, Shear Layer, Square cylinder

Email address: jon.li@cranfield.ac.uk (Zhuoneng Li)

Nomenclature

Greek symbols

Δ	Filter width
ν	Kinematic viscosity (m^2/s)
ω	Weight
Φ	Values of variables
ϕ	basis function
τ	Sub-Grid-Scale tensor
ξ, η, ζ	Coordinates in reference space

Symbols

(x, y, z)	Cartesian coordinates (m)
$\mathbf{F}$	Flux
$\mathbf{L_{is}}$	The length from a cell centre to its face
$\mathbf{n}$	Normal unit vector of a surface
$\mathbf{U}$	Velocity vector (m/s)
a_k	Degrees of freedom
C	Constant
C_d	Drag coefficient (-)
C_l	Lift coefficient (-)
C_p	Pressure coefficient (-)
f_{KH}	Kelvin-Helmholtz frequency
f_{VK}	Von Kármán frequency
K	The number of degrees of freedom
l_R	Reattachment length
p	Pressure (Pa)
Q	Q criterion
Re	Reynolds number (-)

S	Area of a face (m^2)
St	Strouhal number
t	Time (s)
u, v, w	Velocity components
V	Volume of a cell (m^3)
y^+	Non-dimensional spacing normal to the airfoil surface (-)

1. Introduction

The most widely used Computational Fluid Dynamics (CFD) simulation technique in engineering is Reynolds Average Navier-Stokes (RANS) Simulation [1, 2, 3], where a time-space averaging process is applied to the governing equations. Therefore, only averaged quantities are solved where all the instantaneous turbulent motions are modelled by turbulence models. Due to the nature of turbulence, large-scale eddies contain the most turbulent kinetic energy which can be simulated using the Large-Eddy Simulation (LES) method. Within LES, large energy-carrying eddies are resolved directly by the grid whereas small dissipative eddies are accounted for by a Sub-Grid-Scale (SGS) model. In LES, most of the instantaneous flow features are captured with an acceptable computational cost compared with the high fidelity Direct Numerical Simulation (DNS) approach. Therefore the development of more accurate SGS models for LES is motivated since the original contribution from [4] and Drikakis and Rider [5] analysed different SGS models for conventional LES. However, the construction of SGS models for LES is pragmatic, since no universal theory of turbulence is established [6]. The main limitation for this approach is that different SGS models would need to be constructed and calibrated for different flow configurations. Additionally, the complexity of implementing a SGS has limited its popularity [7].

The investigation towards the unconventional LES approach has been encouraged because of aboved mentioned limitations. Boris [8] made one of the first discoveries that the truncation errors of the Flux-Corrected Transport (FCT) algorithm could serve as an SGS model and

he recognised later that several other specially designed algorithms could have the same property as well [9]. By applying modified equation analysis, Fureby and Grinstein [10, 11] have shown that the effect of SGS can be represented by a particular class of flux-limiting algorithms with dissipative leading-order terms. In addition, Grinstein et al. [12, 6] further proved that a particular class of flux-limiting scheme implicitly provides an anisotropic SGS-like model. Due to the absence of explicit SGS models, the group of these numerical methods are generally named Implicit Large-Eddy Simulation (ILES). Following this concept, many similar approaches have been developed and applied extensively to investigate the vortex dynamics and turbulence transition in free shear flows, as demonstrated by Drikakis et al. [7].

Instead of introducing a flux limiter to achieve the goal of producing a non-oscillatory high order solution, the Essentially Non-Oscillatory (ENO) scheme of Harten et al. [13, 14] demonstrates an alternative way by choosing the smoothest of all candidate stencils to avoid spurious oscillations. On the contrary to using one single stencil, the Weighted ENO (WENO) scheme of Liu et al. [15] combines all candidate stencils with a convex weight which is assigned according to the smoothness of the stencil. Therefore, WENO schemes ideally achieve a higher-order of accuracy satisfying the non-linear stability criteria. Initially, WENO schemes were developed for Cartesian grids [16]. Hahn [17] has employed the WENO methods of Balsara and Shu [18] on Taylor Green Vortex (TGV) problem and Hill flow, claiming its efficiency on vortex dynamics and in the shear layer region. Based on the work of [19], Tsoutsanis et al. [20] and Pringuey and Cant [21] have extended the WENO scheme to arbitrary 3-dimensional mixed-element unstructured grids. Promising results are obtained for the simulation of free shear flows in the context of ILES using the open-source package OpenFOAM [22]. More recently, Tsoutsanis et al. [23] further extends the implementation for inviscid flows [20] to viscous flows and assessed the accuracy and efficiency, suggests that the 3rd-order WENO scheme provides the best results in terms of accuracy and computational cost compared with 5th-order WENO and 2nd-order Monotonic Upstream-centered Scheme for Conservation Laws (MUSCL) [24] scheme. The main characteristic of an unstructured WENO scheme, which achieves high order of accuracy in

smooth regions while keeping the non-oscillatory property in sharp gradient regions, makes it particularly attractive in engineering applications that involve higher Reynolds number and more complex physics. Therefore, more validation of this method with benchmark data, particularly on wall bounded flows, should be carried out before it is widely accepted.

The turbulent flow around a square cylinder is a canonical problem for the study of bluff bodies, where significant flow separation occurs around the cylinder. While the separation location of the flow around a circular cylinder is determined by the flow regime of the upstream conditions [25, 26], the separation location of a square cylinder flow is fixed at the upstream sharp corners [27], except for very small Reynolds numbers. Coherent structures of the Von Kármán (VK) and Kelvin-Helmholtz (KH) vortices can be developed on the sides and in the wake region of a square cylinder. The interaction of these two flow structures and the asymmetric shedding vortices in the wake can induce structural vibration to the cylinder, which is known as Vortex-Induced Vibration (VIV) [28]. This phenomenon can also be encountered by other bluff bodies, such as high-rise buildings. Therefore, the focus of many experiments and numerical simulations have been conducted on the square cylinder flow during the last decades.

The first experiment was conducted by Vickery [29], the steady and fluctuating forces of several angles of attack at $Re = 1.0 \times 10^5$ were investigated and the fluctuating lift forces of the square cylinder were found to be three to four times greater than those on the circular cylinder. Following this work, more wind tunnel tests were carried out, as seen in [30, 31, 32]. Based on these initial studies, the characteristics of flow patterns were becoming more clear. For example, the way that the Strouhal number varies with the width-to-height ratio of the cylinders under different Reynolds number [33] and the near wake vortices' evolution [34]. With the increase of computational power, numerical studies on squared cylinder flow emerged with more findings. Saha [35] investigated the flow between $Re = 150$ and 500 and found that the transition from two-dimensional VK vortices to three-dimensional at Re between 150 and 175. The two-dimensional VIV problem of a square cylinder at $Re = 100$ was also investigated by [36]. As LES becomes more accessible, research carried out focussed on turbulent flows with higher Reynolds numbers, particularly at $Re = 22,000$

[37, 38, 39, 40].

High fidelity benchmark data is available for this problem from recent DNS research performed by Trias et al.[41], providing an opportunity to evaluate the performance and efficiency of unstructured WENO scheme in the context of implicit LES and therefore forms the major objective of current research. Considering accuracy and computational cost [23], WENO scheme [42] of second and third order is used. In addition, a conventional SGS-based LES [43] is performed on parallel and the results of near-wall behaviour, time-averaged statistics from both methods are analysed. All the simulations are carried out on the unstructured finite volume based open-source package OpenFOAM V6 so its capability of implicit LES strategy on this particular type of flow is also assessed.

This paper is organized as the following: the basics of the finite volume method within OpenFOAM is introduced in the first section. The following sections include the details of the numerical approach and the discussion of the results from the time-averaged flow and instantaneous flow. Finally, major findings are summarised with the technical contributions.

2. Numerical Approach

2.1. Finite Volume Method in OpenFOAM

Incompressible flows are described by the Navier-Stokes equations:

$$\frac{\partial \mathbf{U}}{\partial t} + \nabla \cdot (\mathbf{U}\mathbf{U}) = -\nabla p + \nu \nabla^2 \mathbf{U}, \tag{1}$$

where $\mathbf{U}$ is the fluid velocity, ν is kinematic fluid viscosity and p is pressure. The incompressibility is satisfied by the continuity equation:

$$\nabla \cdot \mathbf{U} = 0. \tag{2}$$

In the finite volume discretization process, the governing equations are integrated over the finite volumes with arbitrary form. The Gaussian theorem is then applied to transform the volume integrals of the convection and viscous terms into surface integrals. Next, these

surface integrals are treated as discrete ones and evaluated numerically through the use of Gaussian integration. The result is a set of semi-discretized equations:

$$\frac{\partial \overline{\mathbf{U}}_i}{\partial t} + \frac{1}{|V_i|} \sum_{j=1}^{N_{fi}} \int_{S_{fi}} \mathbf{F}(\mathbf{U}) \cdot \mathbf{n}_{fi} dS_{fi} = -(\nabla p)_i \tag{3}$$

$$\sum_{j=1}^{N_{fi}} \int_{S_{fi}} \mathbf{U} \cdot \mathbf{n}_{fi} dS_{fi} = 0, \tag{4}$$

where $|V_i|$ is the volume of a cell, $\mathbf{n}_{fi}$ is the unit vector normal to the surface of discretized element and dS_{fi} is the area, where the subscript fi denotes the index of cell faces. $\overline{\mathbf{U}}_i$ is cell averaged velocity evaluated as:

$$\overline{\mathbf{U}}_i = \frac{1}{|V_i|} \int_{V_i} \mathbf{U} dV, \tag{5}$$

The total flux as the sum of the convection and diffusion fluxes over the face of the element is defined as:

$$\int_{S_{fi}} \mathbf{F}(\mathbf{U}) \cdot \mathbf{n}_{fi} dS_{fi} = \int_{S_{fi}} (\mathbf{U} \cdot \mathbf{n}_{fi} dS_{fi}) \mathbf{U} - \int_{S_{fi}} (\nu \nabla \mathbf{U}) \cdot \mathbf{n}_{fi} dS_{fi}. \tag{6}$$

To evaluate the surface fluxes in Equation (6), a Gaussian quadrature is needed. The integral at the face of the element becomes:

$$\int_S \mathbf{F} \cdot \mathbf{n} dS = \sum_{i=1}^{N_i} (\mathbf{F} \cdot \mathbf{n})_{N_i} \omega_{N_i} S, \tag{7}$$

where i denotes an integration point and N_i is the total number of integration points along the surface. In OpenFOAM, for efficient computation and ease of implementation, one integration point located at the centre (a non-diagonal correction is often applied if centres of adjacent cells are not aligned) of the face is used with a weighting function ω_{N_i} equals to 1. Substituting Equation (6) and Equation (7) into (3) lead to the general form of

semi-discretized governing equations:

$$\frac{\partial \overline{\mathbf{U}}_i}{\partial t} + \frac{1}{|V_i|}\sum_{j=1}^{N_{fi}}(\mathbf{U}_{fi}\cdot\mathbf{S}_{fi})\mathbf{U}_{fi} - \frac{1}{|V_i|}\sum_{j=1}^{N_{fi}}\nu(\nabla\mathbf{U})_{fi}\cdot\mathbf{S}_{fi} = -(\nabla p)_i \tag{8}$$

Note that treatment for pressure gradient $(\nabla p)_i$ is detailed in the following section. The $\mathbf{S}_{fi}$ denotes outward-pointing face area vector for the face fi. To solve above equations, a system of algebraic equations of the form is produced:

$$\begin{pmatrix} a_{11} & a_{12} & \cdots & a_{1n} \\ a_{21} & a_{22} & \cdots & a_{2n} \\ \vdots & \vdots & \ddots & \vdots \\ a_{n1} & a_{n2} & \cdots & a_{nn} \end{pmatrix} \quad \begin{pmatrix} x_1 \\ x_2 \\ \vdots \\ x_n \end{pmatrix} = \begin{pmatrix} b_1 \\ b_2 \\ \vdots \\ b_n \end{pmatrix}$$

$$\mathbf{A}\mathbf{x} = \mathbf{b} \tag{9}$$

Where $\mathbf{A}$ is the coefficient matrix, $\mathbf{x}$ is the solution vector and $\mathbf{b}$ is the vector of boundary conditions and source term. Typically in OpenFOAM, the convective flux $(\mathbf{U}_{fi}\cdot\mathbf{S}_{fi})\mathbf{U}_{fi}$ is always interpolated to cell faces linearly from the adjacent cells. Any available interpolation scheme, such as linear or upwind, TVD-scheme can be applied. The $\mathbf{A}$ Matrix and the $\mathbf{b}$ vector are constructed by the user-selected schemes for every control volume of the domain and is solved iteratively by a user-defined method. OpenFOAM has greatly attracted the attention of engineering and academia, not only because it can provide reliable solutions but also the wide degree of freedoms it can offer its user for customisation.

2.2. LES and ILES framework

The explicit LES equations are obtained by applying a space filter function to Equation (8), we obtain:

$$\frac{\partial \hat{\mathbf{U}}_i}{\partial t} + \frac{1}{|V_i|}[\sum_{j=1}^{N_{fi}}(\hat{\mathbf{U}}\cdot\mathbf{S}_{fi})\hat{\mathbf{U}} - \sum_{j=1}^{N_{fi}}(\nu+\nu_{sgs})(\nabla\hat{\mathbf{U}} + \nabla\hat{\mathbf{U}}^T)\cdot\mathbf{S}_{fi}] = -(\nabla\hat{p})_i \tag{10}$$

For the sake of brevity, the filtered equation is written as:

$$\hat{\mathbf{U}}_t + [\hat{\mathbf{C}} - \hat{\mathbf{V}}] + \hat{\mathbf{P}} = -\nabla \cdot \tau_{sgs}, \tag{11}$$

where $\hat{\mathbf{U}}_t$ is filtered unsteady term, $\hat{\mathbf{C}}$ is filtered convective term, $\hat{\mathbf{V}}$ is filtered viscous term, $\hat{\mathbf{P}}$ is filtered pressure gradient and τ_{sgs} is the unsolved SGS stress and to be closed by a SGS model. Here, the Boussinesq assumption is adpoted to model the SGS stress:

$$\tau_{sgs} - \frac{1}{3}\tau_k \delta = 2\nu_{sgs}\hat{S} \tag{12}$$

$\hat{S}$ denotes the deformation tensor of the resolved field and ν_{sgs} is SGS viscosity to be defined by various formulation. The Wall Adapting Local Eddy Viscosity (WALE) model of Nicoud and Ducros [43], which is well suited for LES involving wall-bounded incompressible flow and unstructured grid, is employed in current research, such that:

$$\nu_{sgs} = C_k k_{sgs} \hat{\Delta} \tag{13}$$

$\hat{\Delta}$ is the filter width equals the cubic root of the cell volume, the constant C_k is set to be 0.094 and the SGS kinetic energy k_{sgs} is calculated based on the square of the velocity gradient tensor. As summarised in [43], due to the property that SGS viscosity would naturally tend to zero in the near-wall region, no damping function is needed to compute the wall-bounded flows. The convective terms $\hat{\mathbf{C}}$ is discretised using Linear-Upwind Stabilised Transport scheme (LUST), where linear-upwind scheme and linear scheme are blended with the fixed coefficient of 0.25 and 0.75. The balance between accuracy and stability on a range of grid quality in the LES context is optimised. Here, the same method is adopted in Cao and Tamura [40].

In terms of the ILES approach, the unresolved turbulent eddies are represented with high-resolution convective schemes when the finite volume discretization method is applied since the original governing equations are replaced by corresponding modified equations hence truncation error terms are introduced during this process. The Modified Equation Analysis

(MEA) suggests that the general form of discretized governing equations is [6]:

$$\mathbf{U}_t + [\mathbf{C} - \mathbf{V}] + \mathbf{P} = \nabla \cdot \tau(\mathbf{U}, \Delta x, \Delta t), \tag{14}$$

The leading truncation error term at the right-hand side is in the form of the divergence of a stress tensor and its similarity to Equation (11) indicates the possibility of ILES approach. For example, as demonstrated by Han [17] the leading truncation error terms for the 3rd-order WENO scheme can be expressed as:

$$\tau = -C\Delta^3 \left|\mathbf{F}'\right| \left(\frac{\partial^2 \mathbf{U}}{\partial x^2}\right)^2 \left(\frac{\partial \mathbf{U}}{\partial x}\right)^{-1} \tag{15}$$

where $\mathbf{F}'$ is the flux Jacobian $\partial\mathbf{F}/\partial\mathbf{U}$.

2.3. Unstructured WENO Scheme

The key points of WENO reconstruction to convective terms of semi-discretised Equations (8) are presented here while the detailed description can be found in Martin and Ivan [42] and Pringuey [22]. Unstructured WENO scheme combines one central stencil and several sector stencils that covers all spatial directions in the vicinity of the targeted cell. The central stencil is built up by adding the neighbour cells of the targeted cell until the desired number of total cells in the stencil is reached, the construction for sector stencils follows a similar logic but with respect to the geometric condition of the cell [20]. The general form of WENO reconstruction is expressed as:

$$p_{WENO}(\xi, \eta, \zeta) = \sum_{m=0}^{N_{Si}} w_m \cdot p_m(\xi, \eta, \zeta), \tag{16}$$

$$w_m = \gamma_m \left(\sum_{m=0}^{N_{Si}} \gamma_m\right)^{-1} \quad \text{with} \quad \gamma_m = \frac{d_m}{(\varepsilon + IS_m)^s}. \tag{17}$$

The reconstruction is carried out in reference space (ξ, η, ζ) to eliminate the scaling effect [19]. In the expression of the nonlinear weights w_m, d_m is the linear weight, $\varepsilon = 10^{-6}$ is a small positive number to prevent the denominator from becoming zero and $s = 4$ is the exponent of the oscillation indicator, aiming to ensure that the contribution of non-smooth

stencils vanishes as the cell size tends to zero. Meanwhile, IS_m is the local smoothness indicator of stencil S_m that smooth solution leads to a smaller IS_m and hence a larger weight. More details can be found in [22] and [44].

The polynomial $p_m(\xi, \eta, \zeta)$ is expressed in a basis of summation of local polynomial functions $\{\phi_k\}_{k=0,\cdots,K}$ in reference space as:

$$p_m(\xi, \eta, \zeta) = \overline{\mathbf{U}}_i + \sum_{k=1}^{K} a_k^{(m)} \phi_k(\xi, \eta, \zeta), \tag{18}$$

where a_k is the degrees of freedom and the number of degrees of freedom K is related to the degree of the polynomial r by the expression:

$$K = \frac{(r+1)(r+2)(r+3)}{6} - 1. \tag{19}$$

The subscript i denotes the cell that is being constructed. To compute the degrees of freedom, a minimum of K cells are needed. In practical however, for the stability of the system, a number of 2K cells are used, as recommended by Olivier and Van Altena [45] and Tsoutsanis et al. [23]. Since the cell-average is not affected by the transformation, it is defined in the reference space as:

$$\overline{\mathbf{U}}_i = \frac{1}{|V_i'|} \int_{V_i'} p(\xi, \eta, \zeta) \mathrm{d}\xi \mathrm{d}\eta \mathrm{d}\zeta, \tag{20}$$

where V_i' is the volume of the mapped cell of V_i. The basis functions ϕ_k must be constructed so that the conservation condition in Equation (20) is satisfied. This implies that the mean value of each basis function over V_i' is zero. With the effort of Gartner et al. [46], the memory demand and efficiency for multi-processor parallel run of the original WENO scheme code for OpenFOAM are greatly optimised.

In OpenFOAM, the value on the cell faces Φ_s are interpolated from cell centres Φ_i. There is a wide range of options for interpolation schemes, such as linear scheme, linear upwind scheme and a hybrid of the linear and linear upwind scheme. These are typically 2nd-order accuracy. The linear upwind scheme is derived from the upwind scheme and returns upwind weighting factors plus a gradient-based explicit correction:

$$\Phi_s = \Phi_i + \mathbf{L}_{is} \nabla \Phi, \tag{21}$$

where $\mathbf{L}_{is}$ is the length from the centre of the cell Φ_i to the cell face Φ_s and $\nabla\Phi$ is calculated based on the difference of face values from 2nd-order linear interpolation and 1st-order upwind scheme. This type of approach that combines a low-order scheme and a higher-order correction term, is called the Deferred Correction approach [47]. The approach enables the use of high order schemes in the codes initially written for lower-order schemes while keeping the stability [48]. Due to the fact that difference of upwind scheme and high order schemes is added as an correction term, the convergence speed may be affected as the difference becomes larger. One technique to overcome the weakness is to introduce a limiting strategy, as described in [42]. Similarly, the WENO polynomials (16) are applied to reconstruct the convective flux terms of (8) on one face of the cell in the reference space [42], we have:

$$\begin{aligned}(\mathbf{U}_{fi}\cdot\mathbf{S}_{fi})\mathbf{U}_{fi} &= \dot{\mathbf{F}}\cdot\sum_{m=0}^{N_{Si}} w_m\cdot p_m(\xi,\eta,\zeta)\\ &= \dot{\mathbf{F}}\cdot\sum_{m=0}^{N_{Si}} w_m\cdot(\overline{\mathbf{U}}_i+\sum_{k=1}^{K} a_k^{(m)}\phi_k(\xi,\eta,\zeta))\\ &= \dot{\mathbf{F}}\cdot(\overline{\mathbf{U}}_i+\sum_{m=0}^{N_{Si}}\sum_{k=1}^{K} w_m a_k^{(m)}\cdot\phi_k(\xi,\eta,\zeta)),\end{aligned} \tag{22}$$

where the $\mathbf{S}_{fi}$ denotes outward-pointing face area vector for the face fi and $\dot{\mathbf{F}}$ denotes the surface normal flux $\mathbf{U}_{fi}\cdot\mathbf{S}_{fi}$ in reference space. Now the convective terms are approximated with an implicit linear scheme and explicit higher-order WENO scheme. The resulting governing equations now take the form:

$$\frac{\partial\overline{\mathbf{U}}_i}{\partial t}+\dot{\mathbf{F}}\cdot(\overline{\mathbf{U}}_i+\sum_{m=0}^{N_{Si}}\sum_{k=1}^{K} w_m a_k^{(m)}\cdot\phi_k(\xi,\eta,\zeta))-\frac{1}{|V_i|}\sum_{j=1}^{N_{fi}}\nu(\nabla\mathbf{U})_{fi}\cdot\mathbf{S}_{fi}=-(\nabla p)_i \tag{23}$$

2.4. Treatment for Gradient Terms

The pressure gradient $-(\nabla p)_i$ in LES Equation (10) and in WENO Equation (23) are calculated in the same approach. Integrating $-(\nabla p)_i$ over a controlled volume V_i then evaluating

with Gaussian mid-point rule:

$$
\begin{aligned}
-(\nabla p)_i &= -\frac{1}{|V_i|}\sum_{j=1}^{N_{fi}}\int_{S_{fi}}(\nabla p)_{fi}\cdot\mathbf{n}_{fi}dS_{fi} \\
&= -\frac{1}{|V_i|}\sum_{j=1}^{N_{fi}}(\nabla p)_{fi}\cdot\mathbf{S}_{fi}
\end{aligned}
\tag{24}
$$

The surface gradient $(\nabla p)_{fi}$ is computed from weighted interpolation of cell centre values $(\nabla p)_P$ and $(\nabla p)_N$:

$$
(\nabla p)_{fi} = f_x(\nabla p)_P + (1-f_x)(\nabla p)_N \tag{25}
$$

Here P denotes the centre of cell i and N denotes the centre of its neighbour and the weight $f_x = \frac{fN}{PN}$. We have further employed a limited non-orthogonal correction method to assure the gradient approximation is 2nd-order accurate despite the possible high degree of non-orthogonality and skewness. The same strategy is applied to the computation for velocity gradient in Equations (10) and (23) therefore it won't be discussed thereafter.

2.5. Temporal Discretization and Time Step

The temporal discretisation is proceed after all the spatial terms are treated. The spacial terms are moved to the right-hand side of the equation denoted RHS:

$$
\frac{\partial\overline{\mathbf{U}}_i}{\partial t} = RHS. \tag{26}
$$

The system is solved by an implicit 2nd-order backward Euler scheme:

$$
\frac{\partial\overline{\mathbf{U}}_i}{\partial t} = \frac{3\overline{\mathbf{U}}_i - 4\overline{\mathbf{U}}_i^{n-1} + \overline{\mathbf{U}}_i^{n-2}}{2\Delta t}, \tag{27}
$$

where n denotes the time step. Note that the order of temporal discretisation does not need to be the same as the order of spatial discretisation, the overall accuracy will be 2nd-order in this paper. According to the DNS study by Trias et al. [41], the smallest Kolmogorov time scale $\tau_\eta = (\nu/\langle\epsilon\rangle)^{(1/2)} \gtrsim 6.8\times10^{-3}$, where $\langle\epsilon\rangle = 2\nu\langle S' : S'\rangle$ is the time-averaged local dissipation of turbulent kinetic energy and $S' = 1/2(\nabla\mathbf{U}' + (\nabla\mathbf{U}')^T)$ is the

fluctuating rate-of-strain tensor. Similar to the conventional LES approach in [40, 49], the non-dimensional time step, $\Delta t^* = \Delta t U/D$, is determined as 1.0×10^{-3} in this ILES study, which yields the maximum Courant number at the fine grid is about 2.4. This time resolution is significantly smaller than the Kolmogorov time scale and close to the DNS time step size. Besides, it also strikes a balance between calculation accuracy and efficiency considering the available computational resources. To investigate time-averaged quantities, approximately 80 shedding cycles were computed in the DNS by Trias et al. [41] and the last 67 cycles were used to obtain the time-averaged field. For the conventional LES approach, the last 13 cycles of a total of 20 cycles are suggested by Voke [50]. A similar number of cycles are used in other explicit LES investigations, such as in [40, 49]. Therefore, we also adopt this number of cycles in our simulations accordingly.

Pressure-Implicit Splitting-Operator (PISO) algorithm is applied to handle the pressure-velocity coupling for each time step for both conventional LES and implicit LES. All the computations are carried out using 4 compute nodes of High-Performance Computing Service of Cranfield University, each computing node has 2 intel E5-2620 v4 (Broadwell) CPUs giving 16 CPU cores and 128GB of shared memory.

2.6. Simulation Setup

The Reynolds number is 22,000 for the test cases, which is calculated as:

$$Re = \frac{UD}{\nu}, \tag{28}$$

where U is the inlet flow velocity, D is the cylinder width and ν is the kinematic viscosity. A schema of the computational domain is shown in Figure 1. The size of the outer boundaries is $30.5D \times 54D \times 4D$, which is similar to the domain of DNS study in [41] ($30.5D \times 54D \times \pi D$) except the length in the span-wise direction. It is reported in several LES investigations [38, 49, 40] that $4D$ in the span-wise direction is more suitable for this case to reduce the correlation of turbulent fluctuations at a separation of one half-period. The length from the inlet to the front face of the cylinder is $10D$, the outlet to the rear face is $19.5D$, and the height of the computational domain is $54D$. These sizes are larger than the common

LES studies [38, 49, 40], ensuring the core flow is less affected by the side boundaries in the cross-stream direction and the wake flow has a longer region to develop in the stream-wise direction.

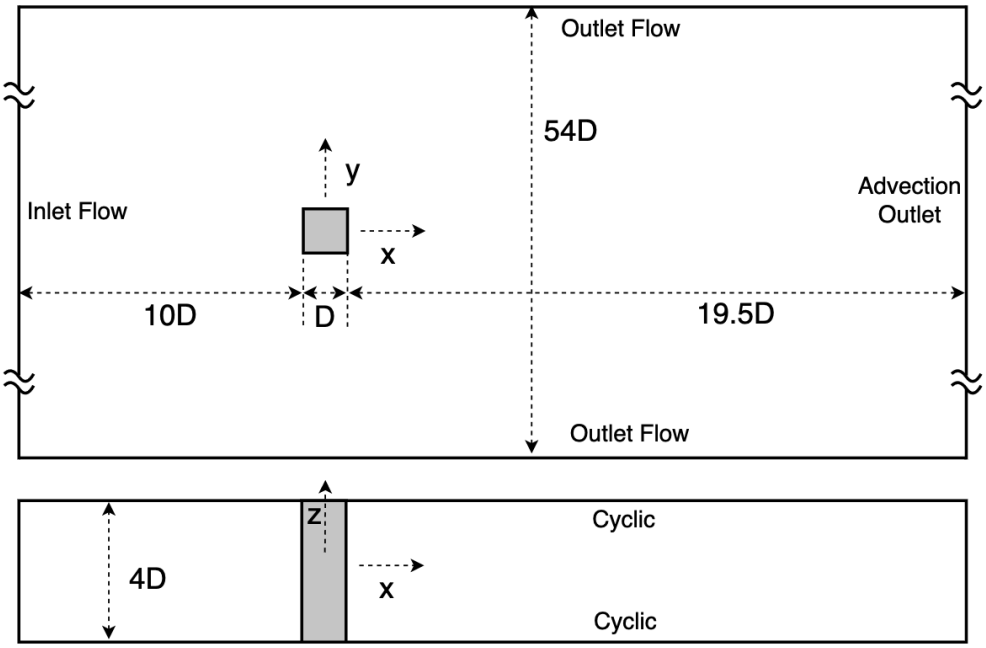

Figure 1: Geometry of the fluid domain

Two wall-resolved and H-O type structured grids with different spacing, named Low Resolution (LR) grid and High Resolution (HR) grid respectively, are generated to investigate the grid effects. Part of the grid information is shown in Table 2. The first height from the square surface of the grids is 6.0×10^{-4}, ensuring the y^+ is smaller than 1.0. In all the three Cartesian system directions, the grid spacing is gradually refined and the number of grid cells is approximately doubled from the LR grid to HR grid, which have 4.15×10^6 and 7.50×10^6 cells respectively. In particular, the grids at the sharp corners of the square and in the wake region are more refined to capture the massive separate flow. The growth ratio in the stream-wise and cross-stream direction is about 1.05. In order to capture the separating shear layer behaviours accurately, extra attention is paid in the span-wise direction, where grid points are equally distributed by $0.0125D$ for the LR grid and $0.01D$ for the HR grid. The spacing meets the requirement for LES simulations suggested by Cao et al. [40] that

the span-wise spacing should be less than $0.02D$. The near wall grid resolution for HR corresponds to (4.3η, 0.43η, 28.6η), where η is the minimum Kolmogorove lenth scale around the cylinder [41]. The grids are shown in Figure 2.

Case	Grid Points	Δy	y^+	$(\Delta x)_{min}$	Δz	Total Cells
LR	$220 \times 240 \times 81$	6.0×10^{-4}	≤ 1.0	1.0×10^{-2}	5.0×10^{-2}	4.15×10^{6}
HR	$270 \times 280 \times 101$	6.0×10^{-4}	≤ 1.0	6.0×10^{-3}	4.0×10^{-2}	7.50×10^{6}
LES Rody [37]	$146 \times 146 \times 20$	-	-	-	-	0.426×10^{6}
LES Minguez [49]	$320 \times 800 \times 128$	-	≤ 6.5	-	5×10^{-1}	3.27×10^{7}
LES Case 2 [40]	$300 \times 300 \times 81$	5.6×10^{-4}	≤ 1.49	-	5×10^{-2}	7.29×10^{6}
DNS Trials [41]	$1272 \times 1174 \times 216$	1.44×10^{-3}	≤ 0.15	1.89×10^{-3}	1.454×10^{-2}	3.22×10^{8}

Table 1: Information of the grids

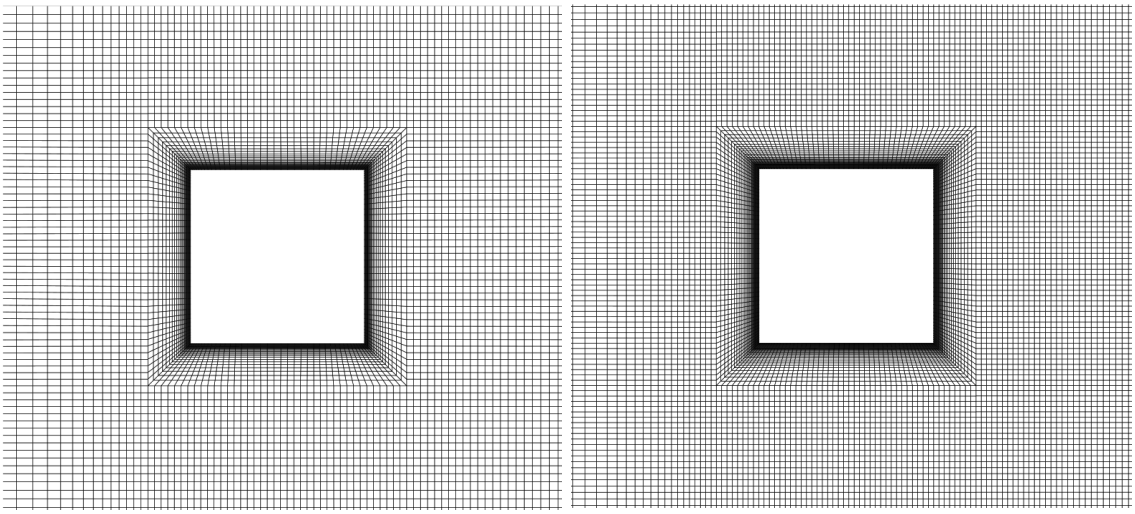

(a) Medium (b) Fine

Figure 2: Grids of the fluid domain

RANS simulations are first conducted for 500 iterations and their results are used as initial conditions. The boundary conditions of the fluid domain are made the same as reference in [41, 40] to stay consistent. A constant velocity profile is imposed at the inlet flow with

$\mathbf{u} = (U, 0, 0)$ where U is determined by the Reynolds number. The outlet boundary is set as the convective condition for the velocity components and pressure. The upper and lower surfaces in the cross-stream direction are given as Neumann boundary condition. No-slip wall condition $\partial \mathbf{u}/\partial y = 0$ is used at the square cylinder surface while the periodic conditions are given at the span-wise faces.

3. Results and discussion

The overall computational time of WENO ILES is more expensive than SGS LES in the current simulations. As summarised in Table 2, on HR grid, the 3rd-order WENO ILES is 3 times more expensive than SGS LES when 64 CPU cores are used. Doubling the number of CPUs can significantly increase the computational efficiency for 3rd-order WENO ILES.

Case	Convective	SGS	CPU cores	CPU Time per time-step
LES LR	LUST	WALE	64	<1
LES HR	LUST	WALE	64	1.4
W2 LR	2nd WENO	-	64	1.3
W2 HR	2nd WENO	-	64	2.2
W3 LR	3nd WENO	-	64	2.5
W3 HR	3nd WENO	-	64/128	4.8/2.5
LES G1 of [40]	LUST	dyamic Smag	240	2-3

Table 2: Summary of Computational Cost

3.1. Time-averaged flow

3.1.1. Comparison of global quantities

The lift and drag coefficients of the square cylinder, C_l and C_d, are recorded with the time evolution in OpenFOAM. The history of the last 100 seconds are shown in Figure 7 and will be discussed later. Here, the time-averaged force coefficients $\langle C_l \rangle$ and $\langle C_d \rangle$, where $\langle \cdot \rangle$

indicates averaged variables, fluctuating force coefficients C_l^{rms} and C_d^{rms}, Strouhal number St and reattachment length l_R of the current study will be first discussed and compared with previous experimental and computational data, as shown in Table 3. First considering the comparison between different grid resolutions, the accuracy of the ILES results compared to DNS data in terms of force fluctuations and l_R has been apparently improved from LR grid to HR grid, despite the order of WENO scheme. For example, 6.6% and 8.3% improvements are obtained for C_d^{rms} and l_R, respectively, by 3rd-order WENO scheme. This is because the filtering process of ILES is implicit and strongly relates to grid scales, finer grids help to capture smaller-scale eddies of turbulence fluctuation and tend to move the reattachment point more upstream. $\langle C_d \rangle$ is slightly improved by grid refinement, only 0.35% improvement is obtained for both WENO scheme orders. Meanwhile, St is only slightly affected by grid resolution and scheme order. Therefore, flow fluctuations are the one that most affected by grid resolution and fine grid can produce more accurate results. In terms of the comparison between different WENO scheme orders, it can be seen that 3rd-order WENO scheme produces more accurate time-averaged quantities compared to DNS data, despite 2nd-order scheme could give acceptable results as well for most of the quantities, such as $\langle C_d \rangle$, C_d^{rms}, St, and l_R. C_l^{rms} gets the most remarkable improvement with 3rd-order WENO scheme. It is reasonable that ILES simulations with higher-order numerical schemes and finer grids have better performance.

Considering the comparison between present ILES study results of the 3rd-order WENO scheme on HR grid and the data from the other three approaches in Table 3, it can be seen that most of the global quantities produced by different studies show great discrepancies. For example, $\langle C_d \rangle$ varies from 2.1 to 2.3, which changes about 9.5%. We speculate this dispersion problem is due to complexity of the flow that is influenced by several factors, such as the explicit SGS model in conventional LES, the implicit model of the convective term in ILES, blockage ratio, grid resolution, and boundary conditions, etc. Despite this, the ILES results are within a reasonable range and very close to the conventional LES data in [40] and current study with HR grid in terms of $\langle C_d \rangle$, St and l_R. Besides, the force fluctuations can be improved up to 17.6% from the above two LES method to ILES approach, which indicates

	Case	$Re/10^3$	$\langle C_d \rangle$	C_d^{rms}	C_l^{rms}	St	l_R
EXP	Lyn et al. [34]	21.4	2.1	-	-	0.133	1.37
	Minguez et al. [49]	21.4	2.1	-	-	0.130	1.37
DNS	Trias et al. [41]	22	2.18	0.205	1.71	0.132	1.04
LES	Minguez et al. [49]	21.4	2.2	-	-	0.141	1.28
	Rodi [37]	22	2.3	0.14	1.15	0.130	1.28
	Cao and Tamura [40]	22	2.21	0.165	1.51	0.133	1.11
	Current LES, HR	22	2.224	0.172	1.527	0.130	1.07
ILES	3rd-order WENO, LR	22	2.284	0.182	1.582	0.130	1.20
	3rd-order WENO, HR	22	2.276	0.194	1.608	0.129	1.10
	2nd-order WENO, LR	22	2.283	0.188	1.418	0.131	1.20
	2nd-order WENO, HR	22	2.275	0.191	1.499	0.130	1.15

Table 3: Comparison between different grid results and previous study results

its potential for strongly separated turbulent flows. However, all of them have a better agreement with DNS data than the LES results by Rodi [37] (a wall model that developed for attached flows is used) in terms of fluctuations. This also could be the use of a coarse grid, which was limited by the computing capability decades ago. Still, good prediction in terms of other global quantities, such as the Strouhal number and reattachment length, were obtained. This also indicates that grid resolution will mainly impact the prediction of fluctuation values. The Strouhal number predicted by most of the studies have a great agreement with each other in a range between 0.13 and 0.133 except for the LES results by Minguez et al. [49] (the wall resolution might not be sufficient for wall resolving method and a special wall treatment method was employed). Moreover, l_R indicates the length of the time-averaged separation region behind the cylinder (see the streamlines in Figure

3b). The ILES and LES studies give upstream positions of reattachment point compared with experimental studies. However, all of them are obviously longer than the DNS data. Overall, the global quantities predicted by the ILES approach are reliable and reasonable. More about C_l^{rms} and C_d^{rms} will be discussed later in section 3.3.1.

3.1.2. Pressure Distribution and Vortex Structure

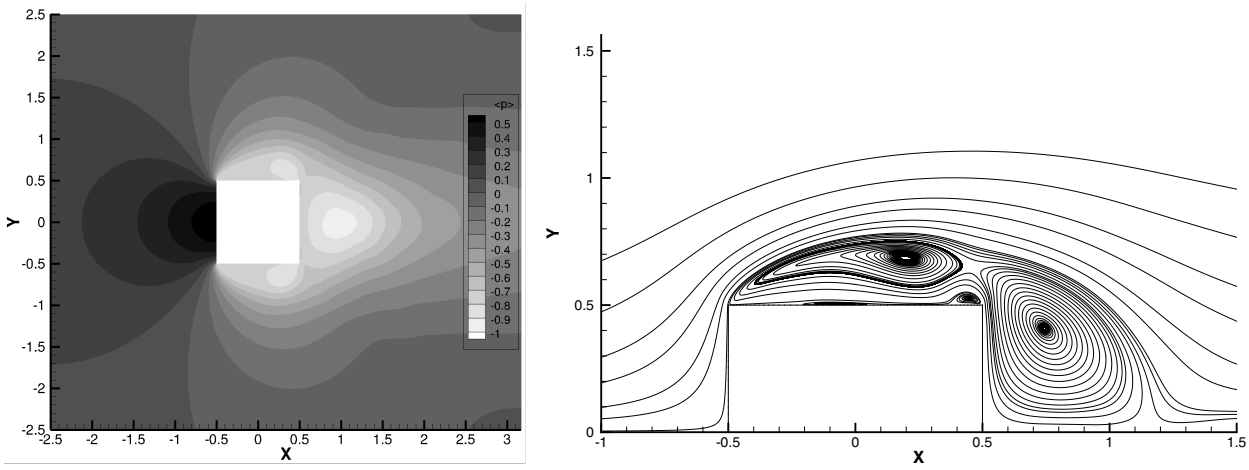

(a) $\langle p \rangle$

(b) Streamline

Figure 3: Time-averaged pressure and streamlines (HR grid)

The time-averaged flow field is obtained by the last 13 vortex shedding cycles. Figure 3 shows the time-averaged pressure field and streamlines. The upstream flow hits to the front surface of the cylinder which significantly reduces the velocity of the flow and rises pressure in this region. This also divides the main flow into two tributaries toward the upper and lower surface, respectively. Then, the front sharp corners force the flow to separate and two large vortices are formed at the top and bottom region, which produces strong pressure gradient and low-pressure regions. Under the large vortex, two secondary vortices are generated near the surface of the cylinder. First, the upstream secondary vortex locates at around $x = -0.1$. This location is further downstream than the DNS data that the upstream vortex is close to the front corner. Meanwhile, this vortex is much weaker than DNS results. Along the upper surface, the pressure is slowly decreasing, as shown in Figure 4 where the time-averaged pressure distribution along the cross-section at the mid-span is displayed. In the area close

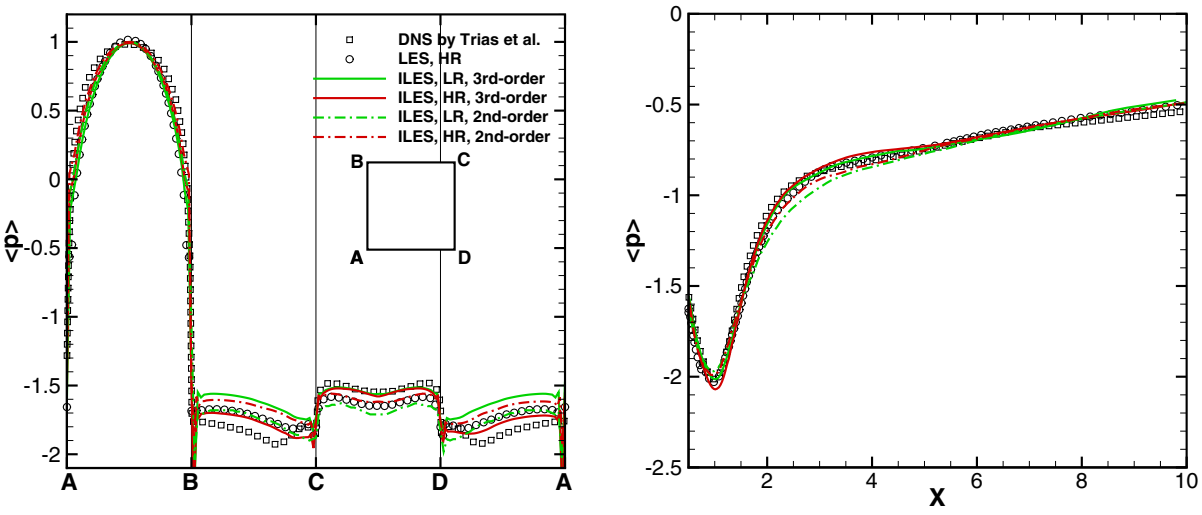

Figure 4: The time-averaged pressure distribution at the cylinder surface and centre line in the wake region (DNS data by Trias et al. [41])

to the downstream corners, another secondary vortex is observed which causes an increase in pressure. However, this pressure increase occurs later and weaker than DNS data. Behind the cylinder, there are a pair of counter-rotating vortex results from the shear-layer which produce a slightly higher pressure region compared to upper and lower surface. The surface pressure distributions of ILES results are compared to conventional LES data obtained by current study and DNS data by Trias et al. [41]. It can be noted that the discrepancy mainly come from the vortex region. DNS gives the largest pressure rise from BC/DA to CD, and the more accurate the numerical method or grid is, the closer the results of ILES are to those of DNS. The 3rd-order WENO scheme on HR grid gives excellent prediction on CD surface and are closest to DNS data on BC/DA surface. The results given by 2nd-order WENO ILES and WALE LES (2nd-order) on the same HR grid are very close to each other. In the wake region, most of the ILES and LES simulations could have good agreement with DNS data in the range of around $1.5D$ behind the cylinder, except for the 2nd-order WENO ILES on LR grid results. However, all of the pressure recovery in the far wake region obtained from the present study are close to each other and slightly faster than the reference data, because the grid spacing is much large in this region and the accuracy is reduced.

3.2. Analysis of Shear Layer Flow

Profiles of the time-averaged velocity and Reynolds stress components in the shear layer region near the cylinder surface is shown in Figure 5 and compared with the DNS and conventional LES data. Generally, the trends of the ILES results have a good agreement with reference data. However, neither ILES nor LES can give satisfactory results in terms of the shear stress profile at $x/D = -0.125$, which is about one order of magnitude below the normal stress. Here, the shear stresses tend to be overestimated in magnitude, meanwhile shows an opposite direction to DNS data within some vertical range. On the other hand, the stream-wise velocity and normal stress profiles of the ILES results show good agreement although these profiles are basically underestimated. The velocity profiles first show a negative value because of the reverse flow of the large vortex, and then turn to positive and gradually accelerated to the maximum of around $1.5m/s$. Besides, the accuracy is also improved with the number of grids increasing. In the region far from the cylinder surface, all results provide great agreement with each other.

Figure 6 shows the normalized and time-averaged velocity components $\langle u \rangle$ and $\langle v \rangle$, the normal stress components $\langle u'u' \rangle$ and $\langle v'v' \rangle$ at five locations of $x = -0.4, -0.2, 0, 0.2, 0.4$ come from the 3rd-order WENO ILES on HR grid. It can be seen that the boundary layer thickness is growing along the cylinder surface and these profiles also have good agreement with DNS data at most of the locations. However, the stream-wise normal stress is underestimated at the front half part of the cylinder. Based on these figures, it can be concluded that the present ILES study could basically provide accurate and reasonable results with the HR grid, but for some very small variables in the shear layer region, the accuracy is obviously reduced.

3.3. Instantaneous Flow

3.3.1. Dynamic Forces

Figure 7 shows the history of the lift and drag coefficient, C_l and C_d, for the last 100 time-units that approximate 13 shedding cycles (HR grid results will be mainly discussed in this section). Figure 8 shows the normalized energy spectra of the force coefficients. It can be

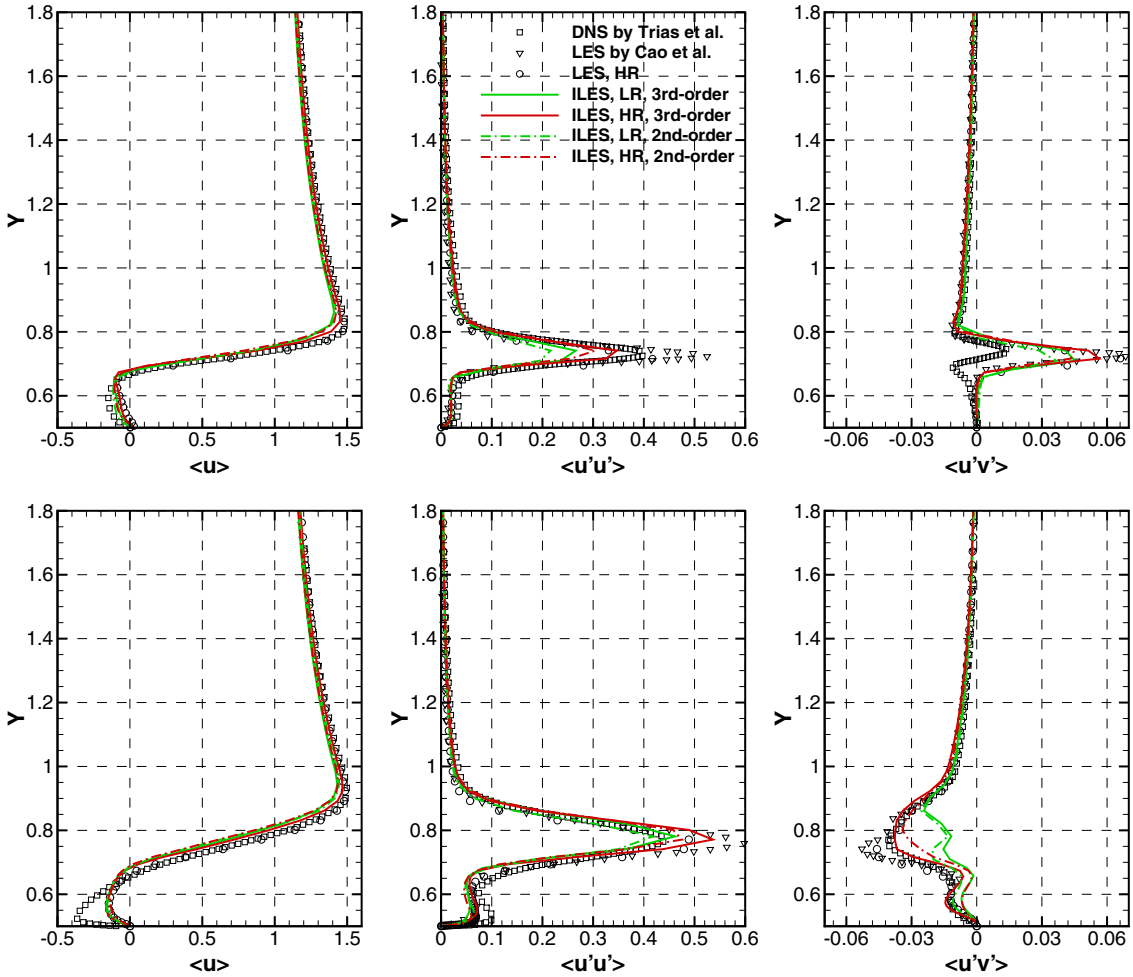

Figure 5: Profiles of $\langle u \rangle$, $\langle u'u' \rangle$, and $\langle u'v' \rangle$ at $x/D = -0.125$ (first row) and $x/D = 0.125$ (second row), compared with the DNS data by Trias et al. [41] LES data by Cao [40] and current study

seen that a clear dominant frequency at 0.130 can be observed for C_l while it is not quite clear for C_d. Several harmonic and sub-harmonic can be observed from the drag coefficient spectra and the peak locates at 0.253 corresponding to the second harmonic. Both the dominant frequency of C_l and peak frequency of C_d are slightly smaller than the DNS data by Trias et al. [41] which are 0.132 and 0.256, respectively. As seen in Table 3, the Strouhal number obtained by different approaches is mainly very close to each other except for the LES data by [49]. The fluctuation of lift and drag coefficients, C_l^{rms} and C_d^{rms}, are 1.608 and 0.194 respectively, which are slightly smaller than the DNS data ($C_l^{rms} = 1.71, C_d^{rms} = 0.205$).

As studied by Trias et al. [41], the fluctuation amplitude might be influenced by the time-integration period. In previous studies [40], the range of C_l^{rms} changes is from 1.15 to 1.79 and from 0.14 to 0.27 for C_l^{rms}. Therefore, the current study has a very good agreement with these reference data.

3.3.2. Instabilities

From the literature, it has been known that the square cylinder flow at $Re = 22,000$ relates to the Kelvin-Helmholtz (KH) instability and Von Kármán vortex. These structures are visualized with the instantaneous magnitude of the pressure gradient, as shown in Figure 9. It can be seen that the resolution of the vortex structure is much lower than the DNS results but they still provide satisfying agreement in terms of vortex structures. These vortices shedding from the cylinder induces force fluctuations as discussed before. Besides, the first KH vortex developed by the front corner is much more downstream than the DNS data that $x/D \approx -4.5$, and more downstream than the conventional LES data by Cao and Tamura [40]. The KH and Von Kármán vortex structure can also be seen by the Q-criterion, as shown in Figure 10. The definition of Q is shown in Equation 29, where $\mathbf{S}$ is the strain and Ω is the rotation tensor.

$$Q = -\frac{1}{2}\left(\|\mathbf{S}\|^2 - \|\Omega\|^2\right). \tag{29}$$

To quantitatively study the dynamics of the cylinder flow, nine monitoring points are created in OpenFOAM and their coordinates are shown in Table 4. All these points are located at the mid-span cross-plane with the first five in the shear layer zone of the top near-wall region while the last four in the wake region. Figure 11 shows the normalized energy spectra of the stream-wise velocity at these points. A clear dominant Strouhal frequency can be seen in the energy spectra of the first three points, which are located near the front corner and also considered as the Von Kármán frequency f_{VK}. But for the two points near downstream corners, S4 and S5, there is no clear dominant frequency can be seen while only several sub-harmonic are observed. This is because the vortices of KH instability have broken into a higher level of turbulence fluctuations in this region while the larger Von Kármán vortices have not been formed yet, hence the turbulent statistics are broadened. This is

Point	x	y	z	Dominant frequency
S1	-0.45	0.63	2.0	0.130
S2	-0.40	0.63	2.0	0.130
S3	-0.30	0.63	2.0	0.130
S4	0.00	0.63	2.0	0.130
S5	0.50	0.63	2.0	0.130
W1	1.00	0.00	2.0	0.253
W2	1.50	0.00	2.0	0.253
W3	2.50	0.00	2.0	0.253
W3	3.50	0.00	2.0	0.253

Table 4: Monitoring point locations

different from the DNS results by Trias et al. [41] that point S5 also shows clear dominate of Von Kármán frequency. Another discrepancy is that the Kelvin-Helmholtz frequency f_{KH} can be observed at point S1, S2, and S3 by the DNS, as well as the conventional LES by Cao and Tamura [40]. However, only point S1 shows a frequency peak at around 5 which indicates the correlation between the frequency of Von Kármán vortex and KH instability $f_{KH}/f_{VK} \approx 38$. This is approximate to the LDV measurement results by Minguez et al. [49] ($f_{KH}/f_{VK} \approx 45$) but smaller than the DNS results ($f_{KH}/f_{VK} \approx 60$). The other four points in the shear layer region do not show clear KH frequency peak. This might because the grid is not fine enough hence too much numerical dissipation are introduced in the shear layer zone and the correlation phenomenon is not well captured.

In the wake region, the flow is mainly characterized by the Von Kármán vortex shedding. The normalized energy spectra of the four points in this region show that the dominant frequency is approximate to the second harmonic Strouhal frequency which is 0.253. Here, the Kolmogorov -5/3 law dominants the inertial range. Moreover, the inertial range tends

to be gradually shortened with the point position goes further downstream which indicates that the level of turbulence is decreasing.

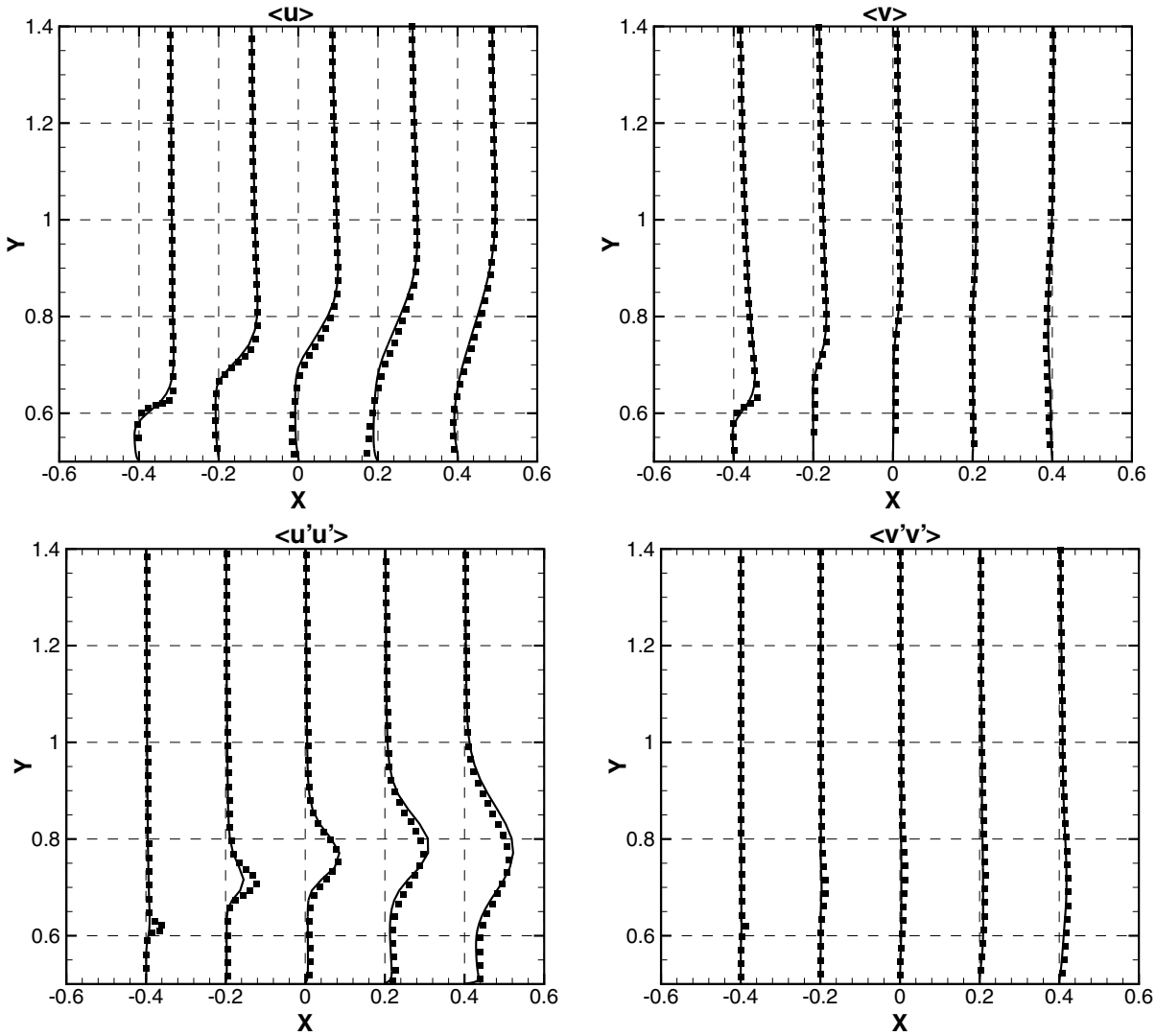

Figure 6: Profiles of the normalized and time-averaged $\langle u \rangle$, $\langle v \rangle$, $\langle u'u' \rangle$ and $\langle v'v' \rangle$ at different locations (3rd-order WENO, HR), compared with the DNS data by Trias et al. [41]

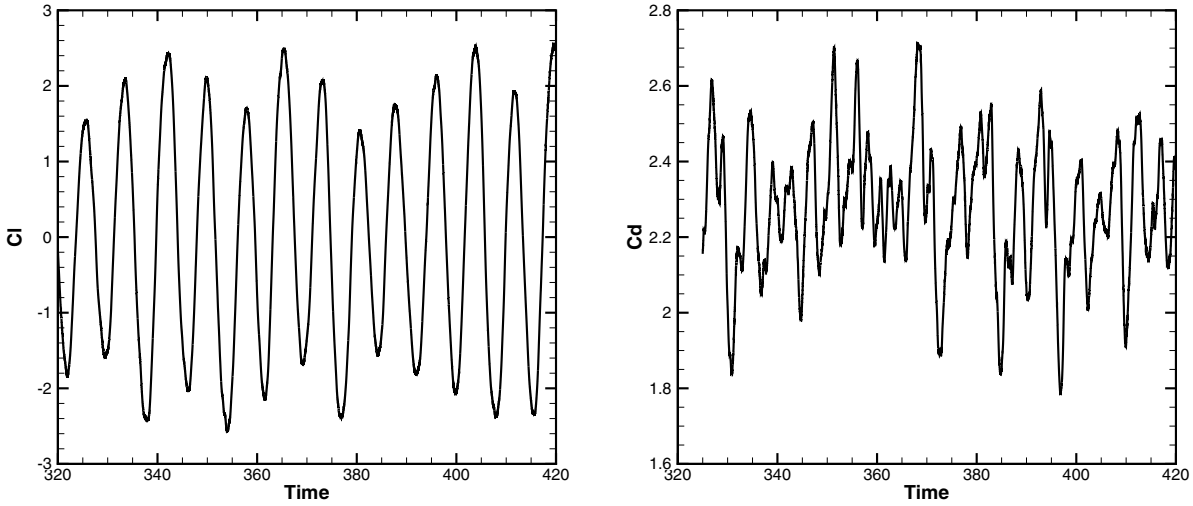

Figure 7: History of force coefficients (HR Grid)

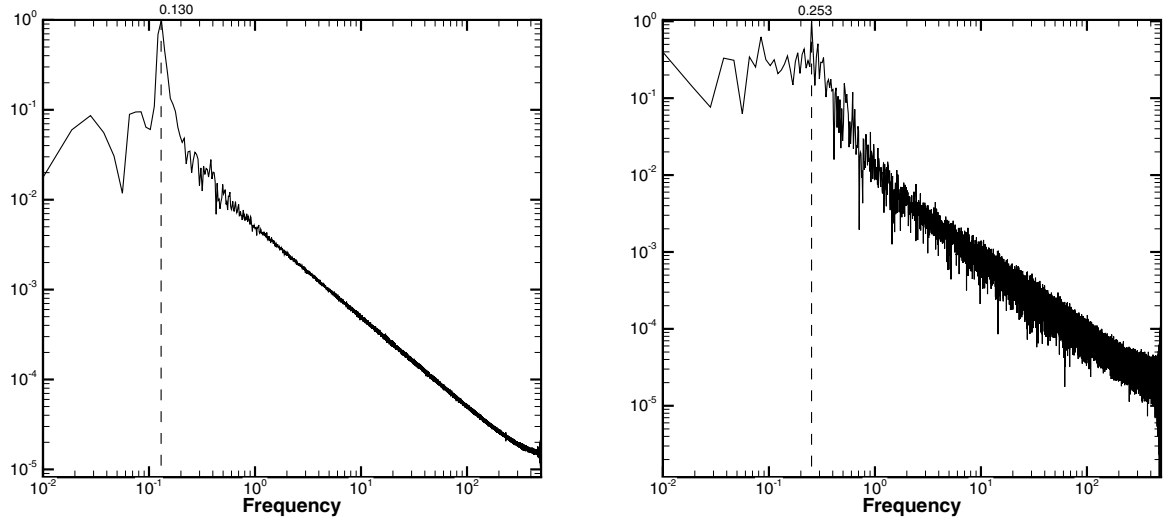

Figure 8: Normalized energy spectra of the force coefficients (HR Grid)

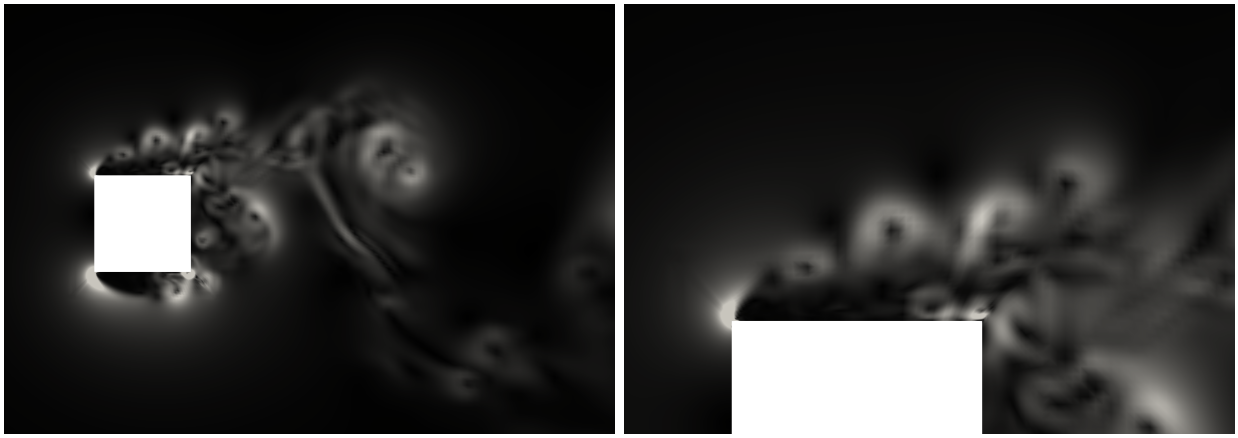

(a) Present ILES study (mid-span cross section)

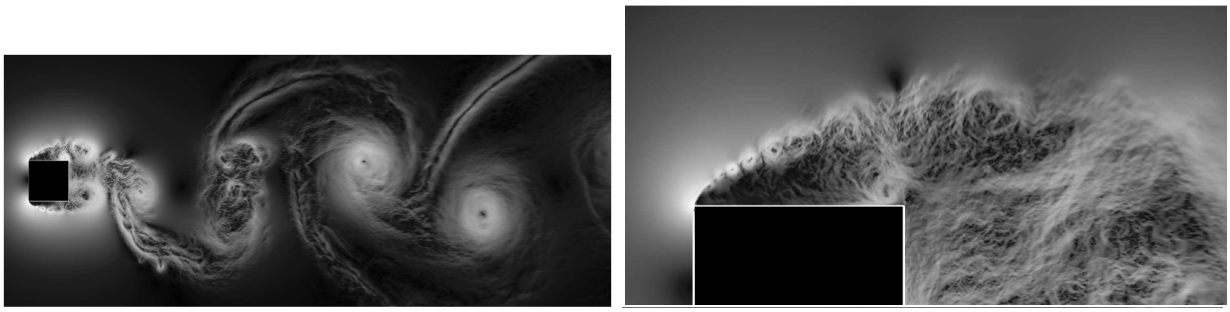

(b) DNS study

Figure 9: Comparison of the KH instability by the instantaneous of pressure gradient between the current ILES study and DNS data [41]

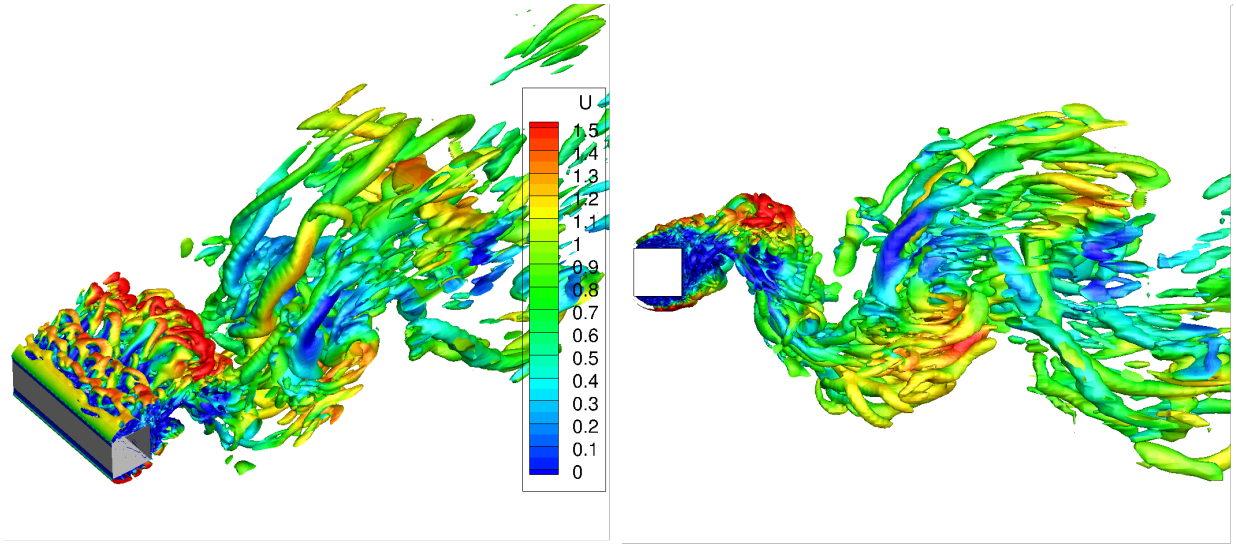

Figure 10: KH and VK vortex structures with Iso-surface of $Q = 0.5$ colored by the streamwise velocity

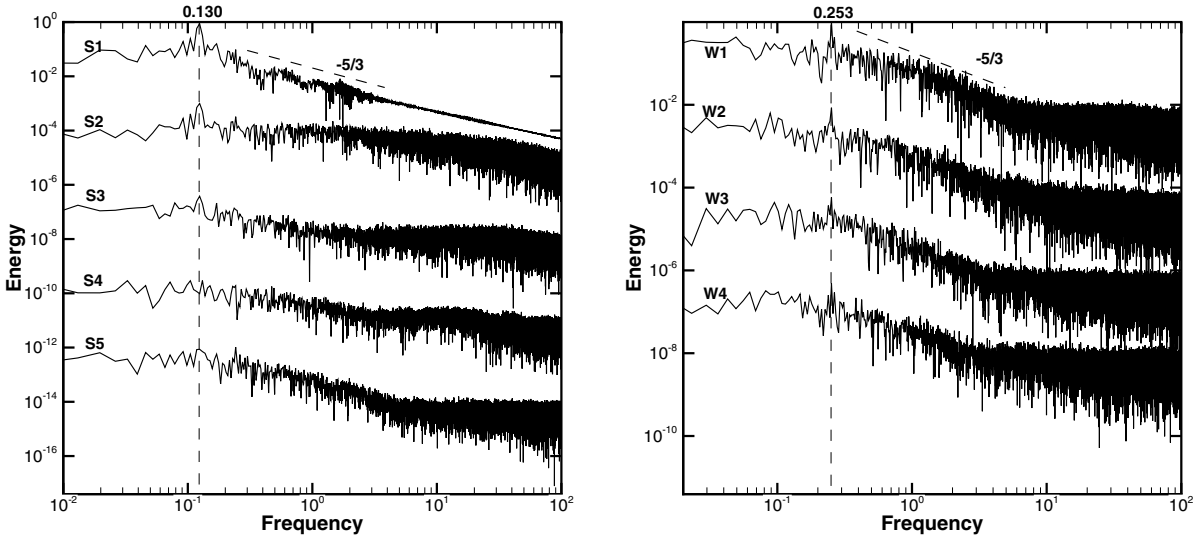

Figure 11: Normalized energy spectra of the stream-wise velocity at the shear layer zone and wake region points

4. Conclusions

The ILES approach with 2nd- and 3rd-order implicit WENO schemes [42] and conventional LES with WALE model are applied to a massively separated square cylinder flow at Reynolds number 22,000 within OpenFOAM. Numerical simulations are performed on a low and high resolution grid ranging from 4.15 to 7.5 million cells with results compared to previous experiments and high fidelity numerical simulations.

For ILES approach, the time-averaged drag coefficient, pressure distribution, velocity profiles and the Reynolds stress components in the shear layer region are in good agreement with reference data. More accurate results are obtained with a finer grid resolution or higher order numerical scheme, especially for the fluctuation quantities and the re-circulation length in wake region. Whereas, the mean values of force coefficients and the Strouhal numbers are hardly impacted by the grid or numerical scheme. The vortex structure of the averaged flow field is well captured, however further work is required in order to predict small quantities such as shear stress.

Further analysis of the instantaneous vortex structures and monitored dynamic variables show that a dominant frequency of lift coefficient exists from the energy spectra. The Von Kármán frequency dominants the region just behind the front corner, whereas no dominant frequency can be seen on the rear half top region because the vortices have broken into a higher level of turbulent fluctuations. The Kelvin-Helmholtz frequency is observed only on the monitor point near to the front corner. In the wake region, the flow is mainly characterized by the Von Kármán vortex shedding and the dominant frequency is similar to the second harmonic Strouhal frequency.

The main findings of this paper are summarised as followed: The unstructured WENO reconstruction scheme implemented in OpenFOAM [42] as the deferred correction approach can produce good results in the context of ILES for turbulent separated flows. The near wall performance of 3rd-order WENO ILES is comparable to the conventional LES with WALE model which is designed for wall bounded flows and out-performs LES with dynamic Smagorinsky model. The computational efficiency can be improved by using more CPU

cores. The 2nd-order WENO scheme can also give a fair prediction over the averaged statistics such as $\langle C_d \rangle$, St, l_R and stream-wise velocity profile with less computational time than a 3rd-order WENO scheme. In the author's opinion, further research is required into the performance of using WENO ILES for practical aerofoils (near stall conditions).

Acknowledgments

This research has extensively employed the Cranfield High Performance Computing (HPC) facility. The authors would like to acknowledge the support and guidance received from Dr Mick Knaggs at the Cranfield HPC department.

References

[1] K. Sakellariou, Z. A. Rana, K. W. Jenkins, Optimisation of the surfboard fin shape using computational fluid dynamics and genetic algorithms, Proceedings of the Institution of Mechanical Engineers, Part P: Journal of Sports Engineering and Technology 231 (4) (2017) 344–354.

[2] D. Expósito, Z. A. Rana, Computational investigations into heat transfer over a double wedge in hypersonic flows, Aerospace Science and Technology 92 (2019) 839–846.

[3] P. Bagul, Z. A. Rana, K. W. Jenkins, L. Könözsy, Computational engineering analysis of external geometrical modifications on MQ-1 unmanned combat aerial vehicle, Chinese Journal of Aeronautics 33 (4) (2020) 1154–1165.

[4] J. Smagorinsky, General Circulation Experiments With the Primitive Equations, Monthly Weather Review 91 (3) (1963) 99–164.

[5] D. Drikakis, W. Rider, High-Resolution Methods for Incompressible and Low-Speed Flows, Springer, 2005.

[6] F. F. Grinstein, L. G. Margolin, W. J. Rider, Implicit Large Eddy Simulation: Computing Turbulent Fluid Dynamics, Cambridge University Press, 2007.

[7] D. Drikakis, C. Fureby, F. F. Grinstein, D. Youngs, Simulation of transition and turbulence decay in the Taylor-Green vortex, Journal of Turbulence 8 (2007) 1–12.

[8] J. P. Boris, On large eddy simulation using subgrid turbulence models Comment 1, in: J. L. Lumley (Ed.), Whither Turbulence? Turbulence at the Crossroads, Springer Berlin Heidelberg, Berlin, Heidelberg, 1990, pp. 344–353.

[9] J. P. Boris, F. F. Grinstein, E. S. Oran, R. L. Kolbe, New insights into large eddy simulation, Fluid Dynamics Research 10 (4-6) (1992) 199–228.

[10] F. F. Grinstein, C. Fureby, Monotonically integrated large eddy simulation of free shear flows, AIAA Journal 37 (5).

[11] C. Fureby, F. F. Grinstein, Large eddy simulation of high-Reynolds-number free and wall-bounded flows, Journal of Computational Physics 181 (1) (2002) 68–97.

[12] F. F. Grinstein, C. Fureby, Implicit large eddy simulation of high-re flows with flux-limiting schemes, 16th AIAA Computational Fluid Dynamics Conference (March 2015).

[13] A. Harten, B. Engquist, S. Osher, S. R. Chakravarthy, Uniformly High Order Accurate Essentially Non-oscillatory Schemes, III, Journal of Computational Physics 131 (1) (1987) 3–47.

[14] A. Harten, S. Osher, Uniformly High-Order Accurate Nonoscillatory Schemes., SIAM Journal on Numerical Analysis 24 (2) (1987) 279–309.

[15] X. D. Liu, Weighted essentially non-oscillatory schemes, Journal of Computational Physics 115 (1) (1994) 200–212.

[16] C.-w. Shu, Essentially Non-Oscillatory and Weighted Essentially Non-Oscillatory Schemes for Hyperbolic Conservation Laws Operated by Universities Space Research Association, ICASE Report (97-65) (1997) 1–78.

[17] M. Hahn, Implicit Large-Eddy Simulation of Low-Speed Separated Flows Using High-Resolution Methods, Cranfield University (2008) 204.

[18] D. S. Balsara, C. W. Shu, Monotonicity preserving weighted essentially non-oscillatory schemes with increasingly high order of accuracy, Journal of Computational Physics 160 (2) (2000) 405–452.

[19] M. Dumbser, M. Käser, Arbitrary high order non-oscillatory finite volume schemes on unstructured meshes for linear hyperbolic systems, Journal of Computational Physics 221 (2) (2007) 693–723.

[20] P. Tsoutsanis, V. A. Titarev, D. Drikakis, WENO schemes on arbitrary mixed-element unstructured meshes in three space dimensions, Journal of Computational Physics 230 (4) (2011) 1585–1601.

[21] T. Pringuey, R. S. Cant, High order schemes on three-dimensional general polyhedral meshes - Application to the level set method, Communications in Computational Physics 12 (1) (2012) 1–41.

[22] T. Pringuey, Large Eddy Simulation of Primary Liquid-Sheet Breakup, Thesis (April).

[23] P. Tsoutsanis, A. F. Antoniadis, D. Drikakis, WENO schemes on arbitrary unstructured meshes for laminar, transitional and turbulent flows, Journal of Computational Physics 256 (2014) 254–276.

[24] B. van Leer, Towards the ultimate conservative difference scheme. V. A second-order sequel to Godunov's method, Journal of Computational Physics 32 (1) (1979) 101–136.

[25] P. Parnaudeau, J. Carlier, D. Heitz, E. Lamballais, Experimental and numerical studies of the flow over a circular cylinder at Reynolds number 3900, Physics of Fluids 20 (8).

[26] C. Norberg, An experimental investigation of the flow around a circular cylinder: Influence of aspect ratio, Journal of Fluid Mechanics 258 (April) (1994) 287–316.

[27] S. Cao, Q. Zhou, Z. Zhou, Velocity shear flow over rectangular cylinders with different side ratios, Computers and Fluids 96 (2014) 35–46.

[28] X. Jiang, Y. Andreopoulos, T. Lee, Z. Wang, Numerical investigations on the vortex-induced vibration of moving square cylinder by using incompressible lattice Boltzmann method, Computers and Fluids 124 (2016) 270–277.

[29] B. J. Vickery, Fluctuating lift and drag on a long cylinder of square cross-section in a smooth and in a turbulent stream, Journal of Fluid Mechanics 25 (3) (1966) 481–494.

[30] B. E. Lee, The effect of turbulence on the surface pressure field of a square prism, Journal of Fluid Mechanics 69 (2) (1975) 263–282.

[31] P. W. Bearman, E. D. Obasaju, An experimental study of pressure fluctuations on fixed and oscillating square-section cylinders, Journal of Fluid Mechanics 119 (1982) 297–321.

[32] C. Norberg, Flow around rectangular cylinders: Pressure forces and wake frequencies, Journal of Wind Engineering and Industrial Aerodynamics 49 (1-3) (1993) 187–196.

[33] Okajima A, Strouhal number of rectangular cylinders, Journal of Fluid Mechanics 123 (1982) 379–398.

[34] D. A. LYN, S. EINAV, W. RODI, J.-H. PARK, A laser-Doppler velocimetry study of ensemble-averaged characteristics of the turbulent near wake of a square cylinder, Journal of Fluid Mechanics 304 (1995) 285–319.

[35] A. K. Saha, G. Biswas, K. Muralidhar, Three-dimensional study of flow past a square cylinder at low Reynolds numbers, International Journal of Heat and Fluid Flow 24 (1) (2003) 54–66.

[36] M. Zhao, L. Cheng, T. Zhou, Numerical simulation of vortex-induced vibration of a square cylinder at a low Reynolds number, Physics of Fluids 25 (2).

[37] W. Rodi, Comparison of LES and RANS calculations of the flow around bluff bodies, Journal of Wind Engineering and Industrial Aerodynamics 69-71 (1997) 55–75.

[38] W. Rodi, J. H. Ferziger, M. Breuer, M. Pourquie, Status of Large Eddy Simulation: Results of a Workshop, Journal of Fluids Engineering 119 (1997) 248–262.

[39] A. Sohankar, L. Davidson, C. Norberg, Large eddy simulation of flow past a square cylinder: Comparison of different subgrid scale models, Journal of Fluids Engineering, Transactions of the ASME 122 (1) (2000) 39–47.

[40] Y. Cao, T. Tamura, Large-eddy simulations of flow past a square cylinder using structured and unstructured grids, Computers and Fluids 137 (2016) 36–54.

[41] F. X. Trias, A. Gorobets, A. Oliva, Turbulent flow around a square cylinder at Reynolds number 22,000: A DNS study, Computers and Fluids 123 (22) (2015) 87–98.

[42] T. Martin, I. Shevchuk, Implementation and validation of semi-implicit WENO schemes using OpenFOAM®, Computation 6 (1) (2018) 1–36.

[43] F. Nicoud, F. Ducros, Subgrid-scale stress modelling based on the square of the velocity gradient tensor, Flow Turbulence and Combustion.

[44] C.-W. Shu, Essentially non-oscillatory and weighted essentially non-oscillatory schemes for hyperbolic conservation laws (97) (1998) 325–432.

[45] C. Ollivier-Gooch, M. Van Altena, A high-order-accurate unstructured mesh finite-volume scheme for the advection-diffusion equation, Journal of Computational Physics 181 (2) (2002) 729–752.

[46] J. W. Gärtner, A. Kronenburg, T. Martin, Efficient WENO library for OpenFOAM, SoftwareX 12 (2020) 100611.

[47] P. K. Khosla, S. G. Rubin, A diagonally dominant second-order accurate implicit scheme, Computers and Fluids 2 (2) (1974) 207–209.

[48] F. Moukalled, L. Mangani, M. Darwish, The finite volume method in computational fluid dynamics : An Advanced Introduction with OpenFOAM and Matlab, Vol. 113, 2016.

[49] M. Minguez, C. Brun, R. Pasquetti, E. Serre, Experimental and high-order LES analysis of the flow in near-wall region of a square cylinder, International Journal of Heat and Fluid Flow 32 (3) (2011) 558–566.

[50] P. VOKE, Flow past a Square Cylinder: Test Case LES2, in: J.-P. Chollet, P. R. Voke, L. Kleiser (Eds.), Direct and Large-Eddy Simulation II, KLUWER ACADEMIC PUBLISHERS, 1997, pp. 355–373.

Declaration of interests

☒ The authors declare that they have no known competing financial interests or personal relationships that could have appeared to influence the work reported in this paper.

☐The authors declare the following financial interests/personal relationships which may be considered as potential competing interests:

Kai Zeng: Literature, Methodology, Post-processing and Writing

Zhuoneng Li: Literature, Methodology, Software and Writing

Zeeshan A. **Rana**: Reviewing and Editing

Karl W. Jenkins: Supervision and Reviewing

2021-05-07

Implicit large eddy simulations of turbulent flow around a square cylinder at Re=22,000

Zeng, Kai

Elsevier

Zeng K, Li Z, Rana ZA, Jenkins KW. (2021) Implicit large eddy simulations of turbulent flow around a square cylinder at Re=22,000. Computers and Fluids, Volume 226, August 2021, Article number 105000

https://doi.org/10.1016/j.compfluid.2021.105000